Mo-$W_{18}O_{49}$/$ZnIn_2S_4$ Composites Synthesized by Metal Doping for Photocatalytic Hydrogen Evolution

Ruiqin Sun , Yue Liu , Jiamei Yang , Tuoya WuRen , Haochen Duan , Zhibing Tan * , Shiyong Yu *

Posted Date: 25 February 2025

doi: 10.20944/preprints202502.1918.v1

Keywords: Visible light; photocatalytic; Mo-$W_{18}O_{49}$; $ZnIn_2S_4$

Article

Mo-$W_{18}O_{49}$/$ZnIn_2S_4$ Composites Synthesized by Metal Doping for Photocatalytic Hydrogen Evolution

Ruiqin Sun[1,†], Yue Liu[2,†], Jiamei Yang[1], Tuoya WuRen[1], Haochen Duan[1], Zhibing Tan[1,*] and Shiyong Yu[1,*]

[1] College of Chemistry and Chemical Engineering, Inner Mongolia University, Hohhot, 010021, China

[2] China FAW Motor Corporation Limited Kinetic Energy Branch, Changchun, 130011, China

* Correspondence: zhibingtan@imu.edu.cn (Z.T.); syyunano@imu.edu.cn (S.Y.)

† These authors contributed equally to this work.

Abstract: Utilizing two or more semiconductor materials with distinct geometric and electronic energy arrangements at the nanoscale to construct heterostructures is an important means for developing high-performance catalysts for photocatalytic hydrogen evolution. In this study, $ZnIn_2S_4$ serves as the primary catalyst carrier, while Mo-$W_{18}O_{49}$ functions as the cocatalyst supported on the surface of $ZnIn_2S_4$. A series of $ZnIn_2S_4$/Mo-$W_{18}O_{49}$ heterojunction composite materials were synthesized through a straightforward hydrothermal method. The $ZnIn_2S_4$/Mo-$W_{18}O_{49}$ photocatalyst demonstrates exceptional photocatalytic hydrogen evolution activity. Notably, with a Mo-$W_{18}O_{49}$ loading of 10%, the photocatalyst achieves optimal hydrogen evolution, yielding 2592.8 μmol g h^{-1}, which is 31 times greater than that of pure $ZnIn_2S_4$. Further characterized results of the samples showed that loading Mo-$W_{18}O_{49}$ with an appropriate mass ratio on $ZnIn_2S_4$ can increase the electron transfer rate, which facilitates reducing the recombination probability of photo-generated electron and holes, thus improve hydrogen evolution efficiency.

Keywords: Visible light; photocatalytic; Mo-$W_{18}O_{49}$; $ZnIn_2S_4$

1. Introduction

Photocatalytic hydrogen evolution is a highly efficient and environmentally friendly method for obtaining hydrogen, therefore, numerous catalysts have been developed for improve the efficiency of this process[1-4]. To date, researchers have identified numerous photocatalysts, including metal oxides such as TiO_2[5,6], ZnO[7], and WO_3[8], as well as g-C_3N_4[9-12] and metal sulfides like CdS[13], ZnS[14], and MoS_2[15]. Recently, ternary metal sulfide compounds, such as $ZnIn_2S_4$[16-18], $Cd_{0.9}Zn_{0.1}S$[19], and $CaIn_2S_4$[20], have been extensively studied due to their unique optical band gaps and good structural stability. Among these, $ZnIn_2S_4$ is notable as the only compound with a layered structure in the metametal sulfide family. Its unit cell consists of three sub-layers: the tetrahedral ZnS_4 surface, the octahedral InS_4 intermediate layer, and another tetrahedral InS_4 bottom layer. This distinctive structure offers advantages for photocatalytic applications[21].

With a hybrid metal sulfide characterized by its monolayer structure, $ZnIn_2S_4$ has garnered significant interest due to its unique architecture and photoelectric properties[22]. It has been proven to possess several advantages, including low toxicity, exceptional absorption of visible light, stability, and an appropriate band gap[23]. However, $ZnIn_2S_4$ exhibits a high recombination rate of photogenerated electrons and holes due to its narrow band gap, and the presence of ultra-thin $ZnIn_2S_4$ nanosheets may lead to spontaneous accumulation and aggregation. Consequently, the performance of $ZnIn_2S_4$ as a catalyst for photocatalytic hydrogen evolution need further optimization. Although $W_{18}O_{49}$ exhibits high chemical stability[24], due to the presence of most oxygen vacancies on the surface, it demonstrate higher overpotentials. which restricts further enhancement of its catalytic performance[25]. Doping is an important method for optimizing semiconductor structures and improving their catalytic capabilities. thus, employing Mo doping to alter the electronic structure of

 doi:10.20944/preprints202502.1918.v1

$W_{18}O_{49}$ may effectively enhance light absorption and improve its optical properties. Consequently, the development of a viable synthesis method for Mo-doped $W_{18}O_{49}$ nanomaterials as efficient hydrogen evolution reaction (HER) catalysts warrants careful consideration.

In this work, $ZnIn_2S_4$ is utilized as the primary catalyst carrier, while Mo-$W_{18}O_{49}$ serves as the cocatalyst, which is deposited onto the surface of $ZnIn_2S_4$. A series of $ZnIn_2S_4$/Mo-$W_{18}O_{49}$ heterojunction composite materials were prepared using a straightforward hydrothermal synthesis method. This distinctive $ZnIn_2S_4$/Mo-$W_{18}O_{49}$ photocatalyst demonstrates excellent photocatalytic hydrogen evolution activity. Notably, with a Mo-$W_{18}O_{49}$ loading of 10%, the photocatalyst achieves optimal hydrogen evolution performance, yielding 2592.8 μmol g h^{-1}, which is 31 times greater than that of pure $ZnIn_2S_4$. Experimental characterization results indicate that the incorporation of Mo-$W_{18}O_{49}$ onto $ZnIn_2S_4$, at an appropriate mass ratio, reduces charge transfer resistance, enhances the electron transfer rate, and facilitates increased electron transport, thereby improving hydrogen evolution efficiency.

2. Results and Discussion

2.1. Characterization of 10% Mo-$W_{18}O_{49}$/$ZnIn_2S_4$ photocatalysts

The crystallographic phases of the prepared pure phase $ZnIn_2S_4$, Mo-$W_{18}O_{49}$, and Mo-$W_{18}O_{49}$/$ZnIn_2S_4$ composites with varying compound proportions were investigated using X-ray diffraction (XRD) patterns. As illustrated in Figure 1, the pure $ZnIn_2S_4$ nanomaterials exhibit distinct diffraction peaks at 27.9°, 33.74°, 47.3°, and 55.5°, corresponding to $ZnIn_2S_4$. These peaks are attributed to the (102), (400), (110), and (202) crystallographic planes, in accordance with the standard card JCPDS No. 72-0773, and are consistent with the reported literature[26-28]. The spectrum of Mo-$W_{18}O_{49}$ reveals diffraction peaks at 23.4° and 26.2°, corresponding to the (010) and (-104) crystal planes, respectively. The XRD pattern of Mo-$W_{18}O_{49}$ aligns with the monoclinic crystal form, with the corresponding standard card being JCPDS No. 71-2450[25,29]. Furthermore, when Mo-$W_{18}O_{49}$ is combined with $ZnIn_2S_4$ to form a composite material, additional diffraction peaks of Mo-$W_{18}O_{49}$ appear in the XRD spectrum alongside the original peaks of $ZnIn_2S_4$. As the loading amount of Mo-$W_{18}O_{49}$ increases, the intensity of these diffraction peaks also rises. Notably, the intensity and width of the XRD peaks for $ZnIn_2S_4$ remain unaffected by the incorporation of Mo-$W_{18}O_{49}$, indicating that the hybridization with Mo-$W_{18}O_{49}$ has minimal impact on the crystallinity and particle size of $ZnIn_2S_4$.

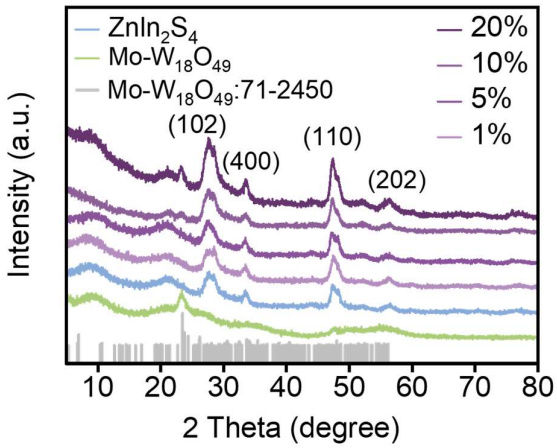

Figure 1. XRD patterns of $ZnIn_2S_4$, Mo-$W_{18}O_{49}$ and Mo-$W_{18}O_{49}$ with loading amount of 1%, 5%, 10%, 20% on $ZnIn_2S_4$.

The morphology and microstructure of pure Mo-$W_{18}O_{49}$, 10% Mo-$W_{18}O_{49}$, and $ZnIn_2S_4$ were examined using scanning electron microscopy (SEM) and transmission electron microscopy (TEM). As illustrated in Figure 2, Mo-$W_{18}O_{49}$ exhibits a sea urchin-like structure formed by the aggregation

 doi:10.20944/preprints202502.1918.v1

of multiple linear structures, with an average particle size of approximately 500 nm. Upon further magnification, Figure 2(c) reveals that Mo-$W_{18}O_{49}$ possesses a branched nanowire structure. Figure 2(d, e) presents a transmission electron micrograph of 10% Mo-$W_{18}O_{49}$/$ZnIn_2S_4$; from this image, it is evident that the sea urchin-like structure of Mo-$W_{18}O_{49}$ is deposited on the surface of $ZnIn_2S_4$ nanoflowers, resulting in a smoother surface, albeit with slight agglomeration, approximately 1 micron in size.

Figure 2(f) displays a high-resolution transmission electron micrograph of 10% Mo-$W_{18}O_{49}$/$ZnIn_2S_4$, where two lattice fringes can be observed at 0.339 nm and 0.32 nm, corresponding to the (-104) surface of Mo-$W_{18}O_{49}$ and the (102) crystal plane of $ZnIn_2S_4$, respectively[30]. Finally, Figures 2(g, h) show scanning electron microscope images of 10% Mo-$W_{18}O_{49}$/$ZnIn_2S_4$, clearly demonstrating that the sea urchin-like material is uniformly coated on the surface of the nanoflower structure. The results from the electron microscope tests indicate that Mo-$W_{18}O_{49}$ and $ZnIn_2S_4$ were successfully combined to form a composite nanomaterial via in-situ deposition. An Energy Dispersive Spectroscopy (EDS) analysis was performed on the composite material to confirm the presence of its constituent elements. The EDS element map (Figure 2 (i-n)) revealed the detection of Mo, W, O, Zn, In, and S. These elements were found to be evenly distributed across the analyzed area. Notably, the lower incorporation levels of Mo, W, and O resulted in a less uniform distribution, which aligns with the experimental observations. These findings robustly demonstrate that the one-pot solvothermal reaction can effectively synthesize 10% Mo-$W_{18}O_{49}$/$ZnIn_2S_4$ composite materials, establishing a strong intimate contact that facilitates the transfer of photogenerated carriers between $ZnIn_2S_4$ and Mo-$W_{18}O_{49}$. This intimate contact may be a critical factor contributing to the enhanced photocatalytic hydrogen evolution activity.

 doi:10.20944/preprints202502.1918.v1

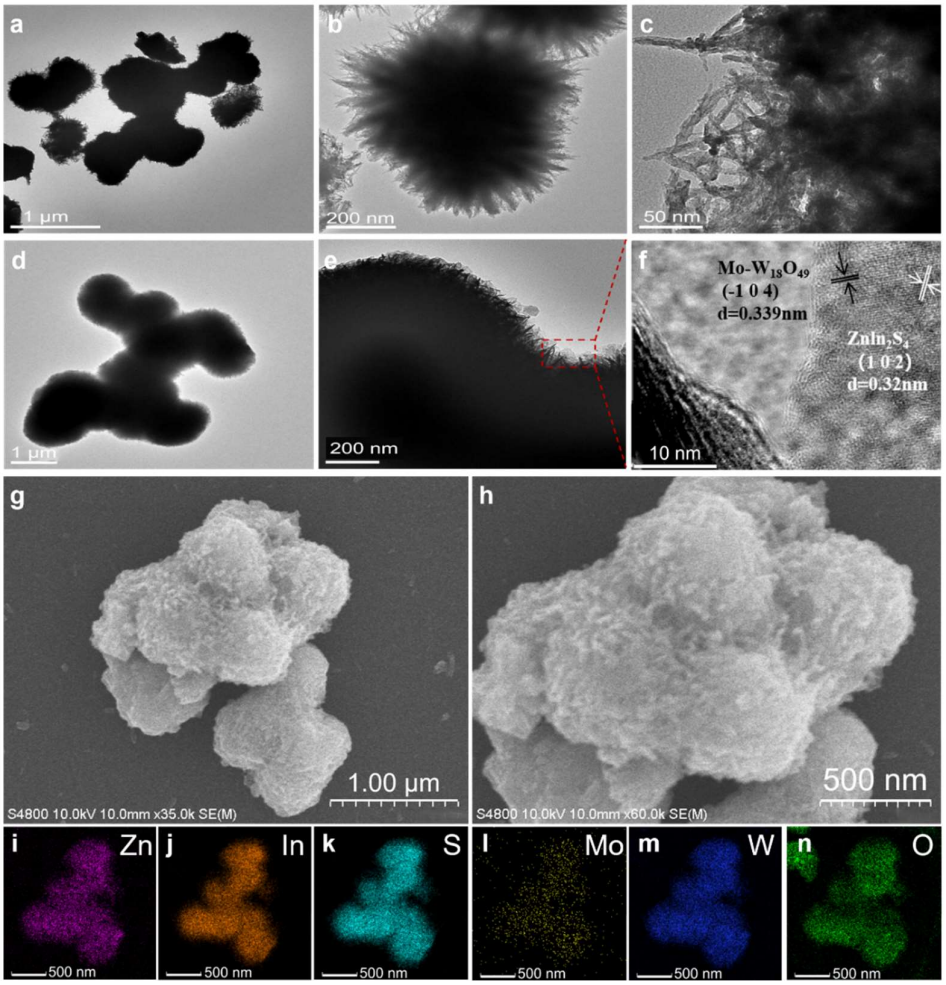

Figure 2. Microstructures of the proposed Mo-$W_{18}O_{49}$ and 10% Mo-$W_{18}O_{49}$/$ZnIn_2S_4$ composites. TEM of Mo-$W_{18}O_{49}$ (a-c) and 10% Mo-$W_{18}O_{49}$/$ZnIn_2S_4$ (d-e), HAADF-STEM images of 10% Mo-$W_{18}O_{49}$/$ZnIn_2S_4$ (f), SEM of 10% Mo-$W_{18}O_{49}$/$ZnIn_2S_4$ (g, h) and EDS elemental results of Zn, In, S, Mo, W, O, (i-n).

The effect of introducing Mo-$W_{18}O_{49}$ on the surface chemical state of $ZnIn_2S_4$ was investigated using X-ray photoelectron spectroscopy (XPS) characterization. Figure 3(a) presents the binding energy spectrum of Zn 2p. It is evident from the figure that pure $ZnIn_2S_4$ exhibits two prominent diffraction peaks at 1023.3 eV and 1046.3 eV, corresponding to Zn $2p_{3/2}$ and Zn $2p_{1/2}$, respectively, which confirms that the valence state of Zn is +2[31]. After the incorporation of Mo-$W_{18}O_{49}$, the peak positions of the two electron binding energies in the composite material shift slightly to lower binding energies, now located at 1022.4 eV and 1045.4 eV, respectively. Figure 3(b) illustrates the binding energy spectrum of In 3d. The pure phase $ZnIn_2S_4$ corresponds to In $3d_{5/2}$ and In $3d_{3/2}$ at binding energy positions of 445.3 eV and 452.9 eV, respectively, indicating that the In element exists as a +3 valence ion[32,33]. Similarly, the binding energy of In3d displays a blue shift following the loading of Mo-$W_{18}O_{49}$. Figure 3(c) presents the high-resolution XPS spectrum of the S element. The XPS spectrum of the pure phase can be fitted into two peaks, corresponding to S $2p_{3/2}$ and S $2p_{1/2}$, confirming the presence of S^{2-}[34,35]. It is apparent from the figure that the diffraction peak of the composite also exhibits a slight shift. As illustrated in Figure 3(d), the high-resolution XPS spectrum of W 4f can be categorized into two pairs of peaks corresponding to W $4f_{7/2}$ and W $4f_{5/2}$, respectively. The peaks at 32.4 eV and 36 eV are associated with W $4f_{5/2}$, while those at 37.7 eV and 38.3 eV correspond to W $4f_{7/2}$. Specifically, the peak at 32.4 eV indicates the presence of +4-valent W, the emission peaks at 36 eV and 37.7 eV signify the existence of +5-valent W, and the peak at 38.3 eV represents +6-valent W[25]. In Figure 3(e), the peak at 531.3 eV corresponds to the bond between

 doi:10.20944/preprints202502.1918.v1

tungsten and oxygen, whereas the peak at 532.9 eV is attributed to the C-O bond. Figure 3(f) shows peaks at 228.3 eV and 231.7 eV, corresponding to the $3d_{5/2}$ and $3d_{3/2}$ states of Mo, respectively, indicating that Mo is doped in the +4 valence state[36]. In summary, the analysis confirms the successful recombination of the two materials. A notable shift in peak positions suggests a significant interface interaction between the two, which facilitates electron transmission. The direction of electron transfer is from $ZnIn_2S_4$ to Mo-$W_{18}O_{49}$.

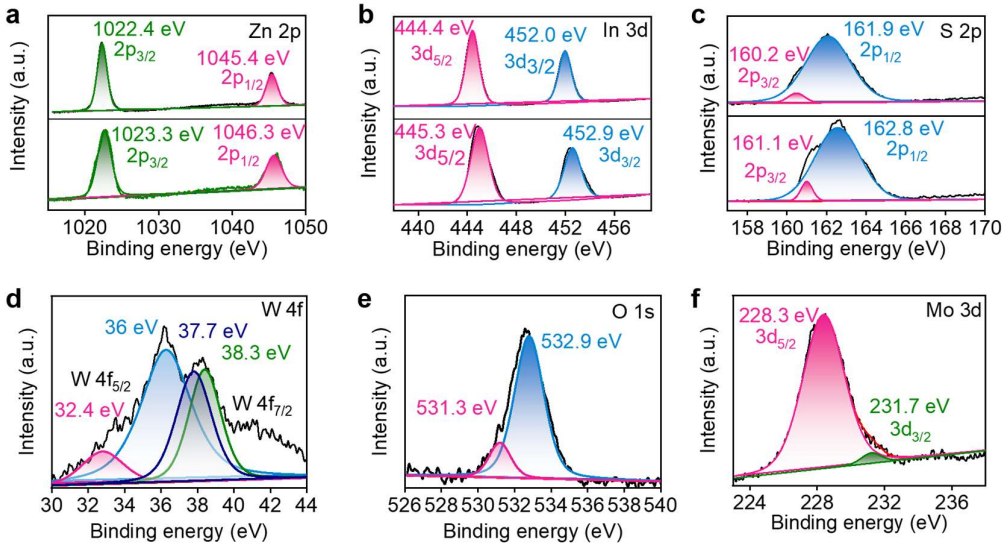

Figure 3. XPS spectra of 10%$ZnIn_2S_4$/Mo-$W_{18}O_{49}$ (a) Zn 2p, top: 10%Mo-$W_{18}O_{49}$/$ZnIn_2S_4$; bottom: $ZnIn_2S_4$. (b) In 3d, top: 10%Mo-$W_{18}O_{49}$/$ZnIn_2S_4$; bottom: $ZnIn_2S_4$. (c) S 2p, top: 10%Mo-$W_{18}O_{49}$/$ZnIn_2S_4$; bottom: $ZnIn_2S_4$. (d) W 4f (e) O 1s (f) Mo 3d.

2.2. Photocatalytic hydrogen evolution performance

The hydrogen evolution activity of the synthesized samples was evaluated through photocatalytic water splitting experiments. Under visible light irradiation, 10 mL of lactic acid was utilized as a catalyst, and the hydrogen evolution activity of various synthesized samples was measured in an aqueous solution containing 90 mL of ultrapure water. Figure 4(a) illustrates that both pure-phase $ZnIn_2S_4$ and composites loaded with varying masses of Mo-$W_{18}O_{49}$/$ZnIn_2S_4$ effectively drive the photocatalytic reduction of water to produce hydrogen under visible light irradiation, with the amount of hydrogen evolution varying among the samples. The cumulative hydrogen evolution of pure $ZnIn_2S_4$ over three hours reached only 83.5 μmol/g. However, by loading Mo-$W_{18}O_{49}$ at different mass ratios, a significant increase in hydrogen evolution was observed. At a loading of 10%, the photocatalyst exhibited optimal hydrogen evolution, yielding 2592.8 μmol/g, which is 31 times greater than that of pure $ZnIn_2S_4$. Conversely, as the loading of Mo-$W_{18}O_{49}$ gradually increased, a decline in photocatalytic hydrogen evolution was noted, likely due to excessive Mo-$W_{18}O_{49}$ coverage on the active sites of $ZnIn_2S_4$. Figure 4(b) presents the photocatalytic hydrogen evolution rate of $ZnIn_2S_4$ and composite materials loaded with different mass ratios of Mo-$W_{18}O_{49}$/$ZnIn_2S_4$. The calculations indicate that the best performance achieved was 864.3 μmol/g. These results are consistent with those shown in Figure 4(a), confirming that the 10% Mo-$W_{18}O_{49}$/$ZnIn_2S_4$ composite catalyst exhibits the highest hydrogen evolution performance.

 doi:10.20944/preprints202502.1918.v1

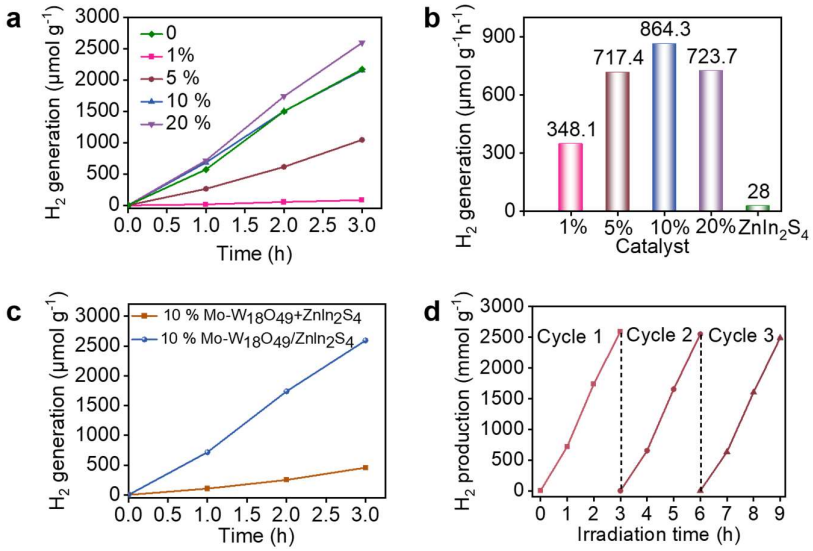

Figure 4. (a) The photocatalytic hydrogen evolution of Mo-$W_{18}O_{49}$/$ZnIn_2S_4$ catalysts with different loadings of Mo-$W_{18}O_{49}$ under visible light irradiation. (b) The photocatalytic hydrogen evolution rate of $ZnIn_2S_4$ and $ZnIn_2S_4$/Mo-$W_{18}O_{49}$ samples under light irradiation. (c) Comparison of photocatalytic hydrogen evolution of 10%Mo-$W_{18}O_{49}$/$ZnIn_2S_4$ catalyst and the same mass of Mo-$W_{18}O_{49}$ $ZnIn_2S_4$ mechanical mixture sample under visible light irradiation. (d) Cycling runs for the photocatalytic hydrogen evolution of the 10%Mo-$W_{18}O_{49}$/$ZnIn_2S_4$ sample under visible light irradiation.

As illustrated in Figure 4(c), a comparison between the 10% Mo-$W_{18}O_{49}$/$ZnIn_2S_4$ sample and the physically mixed sample of Mo-$W_{18}O_{49}$ + $ZnIn_2S_4$, both having the same mass ratio, reveals a significant difference in hydrogen evolution. The hydrogen output from the physically mixed sample is notably lower, being 5.6 times less than that of the 10% Mo-$W_{18}O_{49}$/$ZnIn_2S_4$ sample. This reduction indicates that Mo-$W_{18}O_{49}$ has deposited on $ZnIn_2S_4$ to form a heterojunction structure. Consequently, the composite photocatalyst establishes a close contact interface between Mo-$W_{18}O_{49}$ and $ZnIn_2S_4$, which facilitates charge transfer. This interaction effectively addresses the recombination issue, thereby enhancing photocatalytic hydrogen evolution activity. To evaluate the stability of the composite material, the catalyst exhibiting the best performance was selected for testing cycle performance, as illustrated in Figure 4(d). The reusability of the catalyst was further assessed through three consecutive 3-hour photocatalytic experiments. As shown in Figure 4(d), after three cycles, hydrogen evolution remained stable, with no significant decline, achieving a total of 2488 μmol g^{-1}. Compared to the first cycle, hydrogen evolution in the last two cycles exhibited a slight decrease. This reduction can be attributed to the continuous consumption of the sacrificial agent, which became insufficient during the final two cycles, leading to a decrease in hydrogen yield. Nonetheless, the photocatalyst within this composite material demonstrates commendable stability.

2.3. Explore the mechanism of photocatalytic hydrogen evolution

To investigate the enhanced efficiency of photogenerated carrier separation and transfer in 10% Mo-$W_{18}O_{49}$/$ZnIn_2S_4$ composites, we measured the performance of both pure $ZnIn_2S_4$ and the 10% Mo-$W_{18}O_{49}$ composite under visible light irradiation through multiple on/off cycles. The transient photocurrent response of the $W_{18}O_{49}$/$ZnIn_2S_4$ composite material was analyzed. As illustrated in Figure 5a, the sample generates photocurrent immediately upon illumination, which vanishes instantly when the light source is turned off. After several on/off cycles, the photocurrent response of pure $ZnIn_2S_4$ gradually decreases. In contrast, the 10% Mo-$W_{18}O_{49}$/$ZnIn_2S_4$ composite exhibits a higher and more stable transient photocurrent response, indicating that the incorporation of Mo-$W_{18}O_{49}$ enhances the photocurrent intensity. This synthesized composite material facilitates the

 doi:10.20944/preprints202502.1918.v1

transfer of interface electrons and holes, suggesting that photogenerated electrons are transferred more rapidly. Figure 5(b) presents the electrochemical impedance spectrum, where the semicircle corresponding to the 10% Mo-$W_{18}O_{49}$/$ZnIn_2S_4$ composite is the smallest and has a reduced radius compared to pure $ZnIn_2S_4$. This observation indicates a higher electron transfer rate in the 10% Mo-$W_{18}O_{49}$/$ZnIn_2S_4$ composite. Therefore, the loading of Mo-$W_{18}O_{49}$ onto $ZnIn_2S_4$ at an appropriate mass ratio reduces charge transfer resistance, increases the electron transfer rate, and enables the transport of more electrons, thereby enhancing hydrogen evolution efficiency[37,38].

Photoluminescence (PL) experiments illuminate photocatalysts with light of specific wavelengths, allowing for the acquisition of information related to electronic transitions in the emission spectrum. This further verifies the separation and transfer of electron-hole pairs. Under the excitation of incident light at a wavelength of 250 nm, the photoluminescence performance of $ZnIn_2S_4$ and 10% Mo-$W_{18}O_{49}$/$ZnIn_2S_4$ catalysts was evaluated. As shown in Figure 5(c), $ZnIn_2S_4$ exhibits a pronounced peak at approximately 400 nm, which is attributed to the direct recombination of photogenerated electrons and holes resulting from intrinsic band gap excitation[39]. The figure also indicates that the 10% Mo-$W_{18}O_{49}$/$ZnIn_2S_4$ composite material displays a strong peak around 400 nm; however, the emission intensity of the composite is significantly lower than that of $ZnIn_2S_4$. This observation suggests that the strong interaction at the interface formed between the co-catalysts reduces the recombination efficiency of charges and holes, leading to fluorescence quenching.

To elucidate the photocatalytic mechanism, the Mott-Schottky technique was employed to analyze the samples and determine the sideband positions of $ZnIn_2S_4$ and Mo-$W_{18}O_{49}$, as well as their semiconductor types. As illustrated in Figure 5(d, e), both $ZnIn_2S_4$ and Mo-$W_{18}O_{49}$ exhibit positive slopes in the Mott-Schottky plots, indicating that they are n-type semiconductors[40]. Additionally, the intersection with the X-axis allows for the determination of the sideband positions of $ZnIn_2S_4$ and Mo-$W_{18}O_{49}$. From the data presented in Figure 5(d, e), it can be concluded that the flat band potentials of $ZnIn_2S_4$ and Mo-$W_{18}O_{49}$ are -1.7 eV and -1.2 eV (vs. Ag/AgCl), respectively. Previous studies have shown that the conduction band position (E_{CB}) of an n-type semiconductor is determined by the flat band potential (E_{fb})[41]. Since the E_{CB} of n-type semiconductors is typically 0.1 eV more negative than E_{fb}[42], the conduction band potentials of $ZnIn_2S_4$ and Mo-$W_{18}O_{49}$ are calculated to be -1.8 eV and -1.3 eV, respectively.

Following the series of characterization results, we can further elucidate the mechanism diagram of the composite material Mo-$W_{18}O_{49}$/$ZnIn_2S_4$, as illustrated in Figure 5(f). Under visible light excitation with a wavelength exceeding 420 nm, the primary catalyst $ZnIn_2S_4$ and the cocatalyst Mo-$W_{18}O_{49}$ generate photogenerated electrons and holes at their respective conduction band and valence band positions, owing to their suitable band gaps. Mott-Schottky analysis indicates that the conduction band position of $ZnIn_2S_4$ is more negative than that of Mo-$W_{18}O_{49}$. Consequently, the electrons generated in the conduction band of $ZnIn_2S_4$ are readily transferred to the conduction band of Mo-$W_{18}O_{49}$, leading to the reduction of H^+ in H_2O to form H_2. Additionally, the holes generated in the valence band of Mo-$W_{18}O_{49}$ are transferred to the valence band of $ZnIn_2S_4$, where they are ultimately oxidized and decomposed by the sacrificial agent. This composite enhances the efficiency of photocatalytic hydrogen evolution.

 doi:10.20944/preprints202502.1918.v1

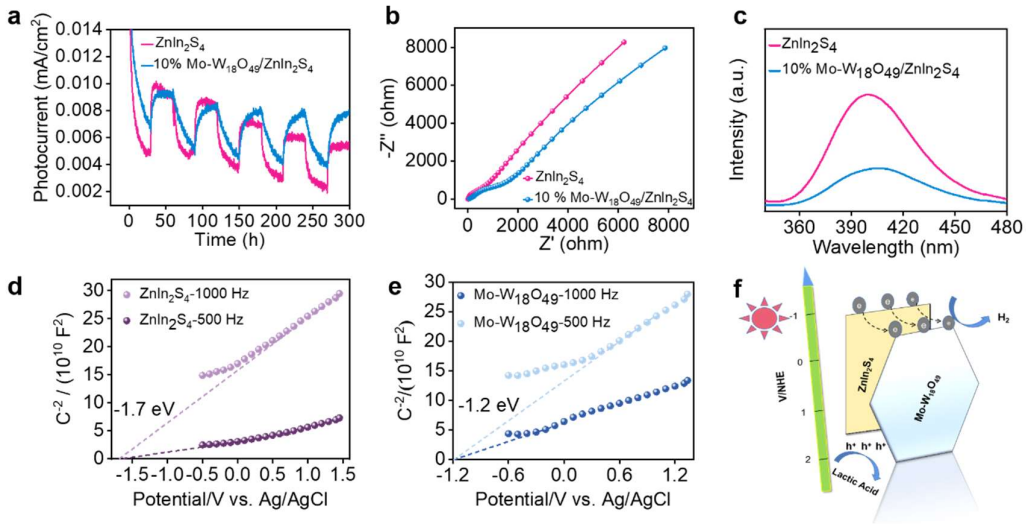

Figure 5. (a) Photocurrent density spectrum of $ZnIn_2S_4$ and 10%Mo-$W_{18}O_{49}$/ $ZnIn_2S_4$. (b) Electrochemical impedance spectroscopy. (c) Photoluminescence spectrum. (d) Mott Schottky plot of $ZnIn_2S_4$ and (e) Mo-$W_{18}O_{49}$. (f) Proposed photocatalytic mrchanism disgram of 10%Mo-$W_{18}O_{49}$/ $ZnIn_2S_4$ composites.

3. Experimental

3.1 Materials and method

To synthesize Mo-$W_{18}O_{49}$, the following procedure was employed: 200 mg of WCl_6 and 40 mg of $MoCl_5$ were dispersed in 70 mL ethanolandstired for 20 min. The resulting mixture was then transferred into a 100 mL Teflon-lined stainles steel autoclave, where it was maintained at 200 °C for 10 h. The products were were subsequently washed repeatedly with deionized water and ethanol. Finally, the samples were dried at 65 °C overnight.

To synthesize $ZnIn_2S_4$/Mo-$W_{18}O_{49}$ composites, 10 mg of Mo-$W_{18}O_{49}$ powder was dissolved in 50 mL of deionized water. Appropriate amounts of $Zn(NO_3)_2{\cdot}6H_2O$ and $In(NO_3)_3{\cdot}4.5H_2O$ were then added to this solution, followed by the adjustment of the pH to 1 using 0.5 M HCl. A specific quantity of thioacetamide, dissolved in 20 mL of deionized water, was slowly introduced to thesolution, while stirring for 1 h. The resulting mixture was transferred into 100 mL a Teflon-lined stainles steel autoclave and maintained at 160 ℃ for 12 h. After this period, the products were washed with deionized water and ethanol, and subsequently dried at 65 ℃. The molar ratios of Mo-$W_{18}O_{49}$ to $ZnIn_2S_4$ were controlled at 1%, 5%, 10%, and 20%, labeled as 1% Mo-$W_{18}O_{49}$/$ZnIn_2S_4$, 5% Mo-$W_{18}O_{49}$/$ZnIn_2S_4$, 10% Mo-$W_{18}O_{49}$/$ZnIn_2S_4$, 20% Mo-$W_{18}O_{49}$/$ZnIn_2S_4$, respectively.

3.2Characterization

The crystal phase properties of the as-prepared products were characterized using X-ray diffraction (XRD, Rigaku, Japan) with Cu-K radiation (λ = 1.5406 Å). The morphology of the samples was examined through scanning electron microscopy (SEM, HITACHI S-4800) and transmission electron microscopy (TEM, FEI Tecnai G2 F20 STwin) at 200 kV. X-ray photoelectron spectroscopy (XPS) analysis was performed using a PHI 5300 ESCA instrument. Additionally, electrochemical impedance spectroscopy (EIS), photocurrent measurements, and Mott–Schottky analysis were conducted on a CHI660E electrochemical workstation.

2.3 Photocatalytic reaction test

The H_2 evolution reactions were conducted using a gas-circulation system (Perfectlight, Beijing). A total of 50 mg of catalyst was dissolved in 90 mL of deionized water and 10 mL of lactic acid. The resulting solution was irradiated with a 300 W xenon lamp equipped with a λ >420 nm cut-off filter.

 doi:10.20944/preprints202502.1918.v1

Nitrogen served as the carrier gas. Ultimately, the quantity of H_2 produced was quantified using gas chromatography (GC7900) with a thermal conductive detector (TCD).

4. Conclusions

Sea urchin-like Mo-$W_{18}O_{49}$ was synthesized using a two-step solvothermal method and subsequently loaded onto the $ZnIn_2S_4$ nanoflower structure to create a $ZnIn_2S_4$/Mo-$W_{18}O_{49}$ heterojunction composite photocatalyst. In this system, $ZnIn_2S_4$ serves as the primary catalyst while Mo-$W_{18}O_{49}$ acts as the Co-catalyst. Under visible light irradiation, electrons generated by the primary catalyst are effectively transferred to the co-catalyst, while holes in the co-catalyst are also efficiently transferred back to the primary catalyst. This process significantly reduces the recombination rate of charge carriers. The Mo-$W_{18}O_{49}$/$ZnIn_2S_4$ heterostructure photocatalyst markedly enhances the photocatalytic performance of $ZnIn_2S_4$ for water splitting and hydrogen evolution under visible light. In the optimal 10% Mo-$W_{18}O_{49}$/$ZnIn_2S_4$ system, the hydrogen generation rate reaches 2592 μmol g^{-1}. The intimate atomic-level contact and strong interaction between $ZnIn_2S_4$ and Mo-$W_{18}O_{49}$ in the composite facilitate efficient electron transfer between the two components, thereby boosting photocatalytic activity. These findings provide a crucial foundation for the design of composite photocatalysts aimed at effective catalytic water splitting for hydrogen evolution.

Supplementary Materials: The following supporting information can be downloaded at the website of this paper posted on Preprints.org.

Author Contributions: Z. T. and S. Y. co-supervised the project. Z. T. and S. Y. convinced the concept and designed the experiments. Z. T., R. S., and Y. L. wrote the manuscript with input from all authors. Y. L. and T. W. prepared the photocatalysts and performed the photocatalytic water splitting experiments and analyzed the data. R. S., Y. L., T. W. and H. D. interpreted the data and developed the discussion. All authors conceived the work and discussed the experiments. All authors have read and agreed to the published version of the manuscript.

Funding: This work was financially supported by the Program of Higher-Level Talents of IMU (No. 21300-5223748), the National Natural Science Foundation of China (No. 22103065, 21661024, 22363008), Young Technology Talent Support Program of Inner Mongolia Autonomous Region Higher Education Institutions (No. NJYT24022), and a Talent Development Fund of Inner Mongolia Province (No. 13100-15112011).

Acknowledgments: The authors are grateful for the instrumental support from the School of Chemistry and Chemical Engineering of Inner Mongolia University.

Conflicts of Interest: The authors declare no conflicts of interest.

References

1. Wang, Y.; Gudiño, L.; Bedia, J.; Belver, C. Solar photocatalytic hydrogen production through metal sulfide/UiO-66-NH_2 heterojunctions. *Sep. Purif. Technol.* **2025**, *353*, 128663. https://doi.org/10.1016/j.seppur.2024.128663.
2. Gong, G.; Liu, Y.; Mao, B.; Tan, L.; Yang, Y.; Shi, W. Ag doping of Zn-In-S quantum dots for photocatalytic hydrogen evolution: simultaneous bandgap narrowing and carrier lifetime elongation. *Appl. Catal. B: Environ.* **2017**, *216*, 11-19. https://doi.org/10.1016/j.apcatb.2017.05.050.
3. Zhang, H.; Shao, C.; Wang, Z.; Zhang, J.; Dai, K. One-step synthesis of seamlessly contacted non-precious metal cocatalyst modified CdS hollow nanoflowers spheres for photocatalytic hydrogen production. *J. Mater. Sci. Technol.* **2024**, *195*, 146-154. https://doi.org/10.1016/j.jmst.2023.11.081.
4. Yang, Z.; Wang, X.; Ren, J.; Xue, Y.; Tian, J. Synergy of atom doping and defect construction in marigold-like $Zn_3In_2S_6$ for improved photocatalytic hydrogen production. *Mater. Today Phys.* **2024**, *46*, 101484. https://doi.org/10.1016/j.mtphys.2024.101484.

 doi:10.20944/preprints202502.1918.v1

5. Li, X.; You, J.; Li, J.; Wang, Z.; Zhao, Y.; Xu, J.; Duan, M.; Zhang, H. Progress of copper-based nanocatalysts in advanced oxidation degraded organic pollutants. *ChemCatChem* **2024**, *16*, *e202301108*. https://doi.org/10.1002/cctc.202301108.
6. Hu, X.; Song, J.; Luo, J.; Zhang, H.; Sun, Z.; Li, C.; Zheng, S.; Liu, Q. Single-atomic Pt sites anchored on defective TiO_2 nanosheets as a superior photocatalyst for hydrogen evolution. *J. Energy Chem.* **2021**, *62*, 1-10. https://doi.org/10.1016/j.jechem.2021.03.003.
7. Dhiman, P.; Rana, G.; Kumar, A.; Sharma, G.; Vo, D.N.; Naushad, M. ZnO-based heterostructures as photocatalysts for hydrogen generation and depollution: a review. *Environ. Chem. Lett.* **2022**, *20*, 1047-1081. https://doi.org/10.1007/s10311-021-01361-1.
8. Xie, X.; Fan, Y.; Tian, W.; Zhang, M.; Cai, J.; Zhang, X.; Ding, J.; Liu, Y.; Lu, S. Construction of Ru/WO_3 with hetero-interface structure for efficient hydrogen evolution reaction. *J. Energy Chem.* **2023**, *83*, 150-157. https://doi.org/10.1016/j.jechem.2023.04.026.
9. Wang, X.; Gong, J.; Dong, Y.; An, S.; Zhang, X.; Tian, J. Energy band engineering of hydroxyethyl group grafted on the edge of 3D g-C_3N_4 nanotubes for enhanced photocatalytic H_2 production. *Mater. Today Phys.* **2022**, *27*, 100806. https://doi.org/10.1016/j.mtphys.2022.100806.
10. Shen, J.; Luo, C.; Qiao, S.; Chen, Y.; Tang, Y.; Xu, J.; Fu, K.; Yuan, D.; Tang, H.; Zhang, H.; et al. Single-atom Cu channel and N-vacancy engineering enables efficient charge separation and transfer between C_3N_4 interlayers for boosting photocatalytic hydrogen production. *ACS Catal.* **2023**, *13*, 6280-6288. https://doi.org/10.1021/acscatal.2c05789.
11. He, F.; Wang, S.; Lu, Y.; Dong, P.; Zhang, Y.; Lin, F.; Liu, X.; Wang, Y.; Zhao, C.; Wang, S.; et al. Unification of hot spots and catalytic sites on isolated boron centers in porous carbon nitride nanosheets for efficient photocatalytic oxygen evolution. *Nano Energy* **2023**, *116*, 108800. https://doi.org/10.1016/j.nanoen.2023.108800.
12. Sun, J.; Yang, J.; Liang, J.; Tu, L.; Bin, Y.; Hou, Y. Construction of microspherical flower-like $Zn_3In_2S_6$-BGQDs/AgBr S-scheme heterojunction for photocatalytic elimination of nitrofurazone and Cr (VI). *Sep. Purif. Technol.* **2022**, *299*, 121563. https://doi.org/10.1016/j.seppur.2022.121563.
13. Zhou, W.; Li, F.; Yang, X.; Yang, W.; Wang, C.; Cao, R.; Zhou, C.; Tian, M. Peanut-chocolate-ball-inspired construction of the interface engineering between CdS and intergrown Cd: boosting both the photocatalytic activity and photocorrosion resistance. *J. Energy Chem.* **2023**, *76*, 75-89. https://doi.org/10.1016/j.jechem.2022.09.013.
14. Huang, R.; Qin, Z.; Shen, L.; Lv, G.; Tao, F.; Wang, J.; Gao, Y. Interface engineering of InP/ZnS core/shell quantum dots by the buffer monolayer for exceptional photocatalytic H_2 evolution. *J. Mater. Chem. A* **2023**, *11*, 6217-6225. https://doi.org/10.1039/D3TA00168G.
15. Li, Z.; Li, C.; Chen, J.; Xing, X.; Wang, Y.; Zhang, Y.; Yang, M.; Zhang, G. Confined synthesis of MoS_2 with rich Co-doped edges for enhanced hydrogen evolution performance. *J. Energy Chem.* **2022**, *70*, 18-26. https://doi.org/10.1016/j.jechem.2022.01.001.
16. Su, L.; Wang, P.; Wang, J.; Zhang, D.; Wang, H.; Li, Y.; Zhan, S.; Gong, J. Pt–Cu interaction induced construction of single Pt sites for synchronous electron capture and transfer in photocatalysis. *Adv. Funct. Mater.* **2021**, *31*, *2104343*. https://doi.org/10.1002/adfm.202104343.
17. Lu, Y.; Jia, X.; Ma, Z.; Li, Y.; Yue, S.; Liu, X.; Zhang, J. W^{5+}–W^{5+} pair induced LSPR of $W_{18}O_{49}$ to sensitize $ZnIn_2S_4$ for full-spectrum solar-light-driven photocatalytic hydrogen evolution. *Adv. Funct. Mater.* **2022**, *32*, *2203638*. https://doi.org/10.1002/adfm.202203638.
18. Du, C.; Yan, B.; Lin, Z.; Yang, G. Enhanced carrier separation and increased electron density in 2D heavily N-doped $ZnIn_2S_4$ for photocatalytic hydrogen production. *J. Mater. Chem. A* **2020**, *8*, 207-217. https://doi.org/10.1039/C9TA11318E.
19. Kang, F.; Shi, C.; Zhu, Y.; Eqi, M.; Shi, J.; Teng, M.; Huang, Z.; Si, C.; Jiang, F.; Hu, J. Dual-functional marigold-like Zn Cd1-xS homojunction for selective glucose photoreforming with remarkable H_2 coproduction. *J. Energy Chem.* **2023**, *79*, 158-167. https://doi.org/10.1016/j.jechem.2022.11.043.
20. Bariki, R.; Kumar Pradhan, S.; Panda, S.; Kumar Nayak, S.; Majhi, D.; Das, K.; Mishra, B.G. In-situ synthesis of structurally oriented hierarchical UiO-66(–NH_2)/$CdIn_2S_4$/$CaIn_2S_4$ heterostructure with dual S-scheme

 doi:10.20944/preprints202502.1918.v1

engineering for photocatalytic renewable H_2 production and asulam degradation. *Sep. Purif. Technol.* **2023**, *314*, 123558. https://doi.org/10.1016/j.seppur.2023.123558.

21. Janani, R.; Preethi V, R.; Singh, S.; Rani, A.; Chang, C. Hierarchical ternary sulfides as effective photocatalyst for hydrogen generation through water splitting: a review on the performance of $ZnIn_2S_4$. *Catalysts* **2021**, *11*, 277. https://doi.org/10.3390/catal11020277.
22. Luan, J.; Chen, J. Photocatalytic water splitting for hydrogen production with novel Y_2MSbO_7 (M = Ga, In, Gd) under visible light irradiation. *Materials* **2012**, *5*, 2423-2438. https://doi.org/10.3390/ma5112423.
23. Zhang, Z.; Huang, L.; Zhang, J.; Wang, F.; Xie, Y.; Shang, X.; Gu, Y.; Zhao, H.; Wang, X. In situ constructing interfacial contact $MoS_2/ZnIn_2S_4$ heterostructure for enhancing solar photocatalytic hydrogen evolution. *Appl. Catal. B: Environ.* **2018**, *233*, 112-119. https://doi.org/10.1016/j.apcatb.2018.04.006.
24. Li, A.; Peng, Z.; Fu, X. Exfoliated, mesoporous $W_{18}O_{49}$/g-C_3N_4 composites for efficient photocatalytic H_2 evolution. *Solid State Sci.* **2020**, *106*, 106298. https://doi.org/10.1016/j.solidstatesciences.2020.106298.
25. Zhong, X.; Sun, Y.; Chen, X.; Zhuang, G.; Li, X.; Wang, J.G. Mo doping induced more active sites in urchin-like $W_{18}O_{49}$ nanostructure with remarkably enhanced performance for hydrogen evolution reaction. *Adv. Funct. Mater.* **2016**, *26*, 5778-5786. https://doi.org/10.1002/adfm.201601732.
26. Gao, Y.; Xu, B.; Cherif, M.; Yu, H.; Zhang, Q.; Vidal, F.; Wang, X.; Ding, F.; Sun, Y.; Ma, D.; et al. Atomic insights for ag interstitial/substitutional doping into $ZnIn_2S_4$ nanoplates and intimate coupling with reduced graphene oxide for enhanced photocatalytic hydrogen production by water splitting. *Appl. Catal. B: Environ.* **2020**, *279*, 119403. https://doi.org/10.1016/j.apcatb.2020.119403.
27. Pudkon, W.; Kaowphong, S.; Pattisson, S.; Miedziak, P.J.; Bahruji, H.; Davies, T.E.; Morgan, D.J.; Hutchings, G.J. Microwave synthesis of $ZnIn_2S_4/WS_2$ composites for photocatalytic hydrogen production and hexavalent chromium reduction. *Catal. Sci. Technol.* **2019**, *9*, 5698-5711. https://doi.org/10.1039/c9cy01553a.
28. Bo, L.; He, K.; Tan, N.; Gao, B.; Feng, Q.; Liu, J.; Wang, L. Photocatalytic oxidation of trace carbamazepine in aqueous solution by visible-light-driven $ZnIn_2S_4$: performance and mechanism. *J. Environ. Manage.* **2017**, *190*, 259-265. https://doi.org/10.1016/j.jenvman.2016.12.050.
29. Bhavani, P.; Praveen Kumar, D.; Jeong, S.; Kim, E.H.; Park, H.; Hong, S.; Gopannagari, M.; Amaranatha Reddy, D.; Song, J.K.; Kim, T.K. Multidirectional-charge-transfer urchin-type Mo-doped $W_{18}O_{49}$ nanostructures on CdS nanorods for enhanced photocatalytic hydrogen evolution. *Catal. Sci. Technol.* **2018**, *8*, 1880-1891. https://doi.org/10.1039/C7CY02162C.
30. Zou, X.; Yuan, C.; Cui, Y.; Dong, Y.; Chen, D.; Ge, H.; Ke, J. Construction of zinc-indium-sulfide/indium oxide step-scheme junction catalyst for enhanced photocatalytic activities of pollutant degradation and hydrogen generation. *Sep. Purif. Technol.* **2021**, *266*, 118545. https://doi.org/10.1016/j.seppur.2021.118545.
31. Zhang, Z.; Huang, L.; Zhang, J.; Wang, F.; Xie, Y.; Shang, X.; Gu, Y.; Zhao, H.; Wang, X. In situ constructing interfacial contact $MoS_2/ZnIn_2S_4$ heterostructure for enhancing solar photocatalytic hydrogen evolution. *Appl. Catal. B: Environ.* **2018**, *233*, 112-119. https://doi.org/10.1016/j.apcatb.2018.04.006.
32. Xiong, M.; Chai, B.; Yan, J.; Fan, G.; Song, G. Few-layer WS_2 decorating $ZnIn_2S_4$ with markedly promoted charge separation and photocatalytic H_2 evolution activity. *Appl. Surf. Sci.* **2020**, *514*, 145965. https://doi.org/10.1016/j.apsusc.2020.145965.
33. Zhao, C.; Zhang, Y.; Jiang, H.; Chen, J.; Liu, Y.; Liang, Q.; Zhou, M.; Li, Z.; Zhou, Y. Combined effects of octahedron NH_2 -UiO-66 and flowerlike $ZnIn_2S_4$ microspheres for photocatalytic dye degradation and hydrogen evolution under visible light. *J. Phys. Chem. C* **2019**, *123*, 18037-18049. https://doi.org/10.1021/acs.jpcc.9b03807.
34. Gao, Z.; Chen, K.; Wang, L.; Bai, B.; Liu, H.; Wang, Q. Aminated flower-like $ZnIn_2S_4$ coupled with benzoic acid modified g-C_3N_4 nanosheets via covalent bonds for ameliorated photocatalytic hydrogen generation. *Appl. Catal. B: Environ.* **2020**, *268*, 118462. https://doi.org/10.1016/j.apcatb.2019.118462.
35. Ye, L.; Fu, J.; Xu, Z.; Yuan, R.; Li, Z. Facile one-pot solvothermal method to synthesize sheet-on-sheet reduced graphene oxide (RGO)/$ZnIn_2S_4$ nanocomposites with superior photocatalytic performance. *ACS Appl. Mater. Interfaces* **2014**, *6*, 3483-3490. https://doi.org/10.1021/am5004415.
36. Xiong, M.; Yan, J.; Chai, B.; Fan, G.; Song, G. Liquid exfoliating CdS and MoS_2 to construct 2D/2D MoS_2/CdS heterojunctions with significantly boosted photocatalytic H_2 evolution activity. *J. Mater. Sci. Technol.* **2020**, *56*, 179-188. https://doi.org/10.1016/j.jmst.2020.03.037.

37. Ren, D.; Shen, R.; Jiang, Z.; Lu, X.; Li, X. Highly efficient visible-light photocatalytic H_2 evolution over 2D–2D CdS/Cu_7S_4 layered heterojunctions. *Chin. J. of Catal.* **2020**, *41*, 31-40. https://doi.org/10.1016/S1872-2067(19)63467-4.
38. Wang, K.; Li, Y.; Li, J.; Zhang, G. Boosting interfacial charge separation of $Ba_5Nb_4O_{15}$/g-C_3N_4 photocatalysts by 2D/2D nanojunction towards efficient visible-light driven H_2 generation. *Appl. Catal. B: Environ.* **2020**, *263*, 117730. https://doi.org/10.1016/j.apcatb.2019.05.032.
39. Li, C.; Che, H.; Yan, Y.; Liu, C.; Dong, H. Z-scheme $AgVO_3$/$ZnIn_2S_4$ photocatalysts: "one stone and two birds" strategy to solve photocorrosion and improve the photocatalytic activity and stability. *Chem. Eng. J.* **2020**, *398*, 125523. https://doi.org/10.1016/j.cej.2020.125523.
40. Mishra, P.; Acharya, L.; Parida, K. A comparison study between novel ternary retrieval $NiFe_2O_4$@p-doped g-C_3N_4 and Fe_3O_4@p-doped g-C_3N_4 nanocomposite in the field of photocatalysis, H_2 energy production and super capacitive property. *Mater. Today: Proceedings* **2021**, *35*, 281-288. https://doi.org/10.1016/j.matpr.2020.05.764.
41. Yang, C.; Li, Q.; Xia, Y.; Lv, K.; Li, M. Enhanced visible-light photocatalytic CO_2 reduction performance of $ZnIn_2S_4$ microspheres by using CeO_2 as cocatalyst. Appl. Surf. Sci. 2019, 464, 388-395. https://doi.org/10.1016/j.apsusc.2018.09.099.
42. Guo, W.; Lian, X.; Nie, Y.; Hu, M.; Wu, L.; Gao, H.; Wang, T. Facile growth of β-$Cu_2V_2O_7$ thin films and characterization for photoelectrochemical water oxidation. Mater. Lett. 2020, 258, 126842. https://doi.org/10.1016/j.matlet.2019.126842.NE.Bib